



Article

Wood Decay Detection in Norway Spruce Forests Based on Airborne Hyperspectral and ALS Data

Michele Dalponte ^{1,*}, Alvar J. I. Kallio ², Hans Ole Ørka ², Erik Næsset ² and Terje Gobakken ²¹ Research and Innovation Centre, Fondazione E. Mach, Via E. Mach 1, 38098 San Michele all'Adige, Italy² Faculty of Environmental Sciences and Natural Resource Management, Norwegian University of Life Sciences, P.O. Box 5003, NO-1432 Ås, Norway; alvar.j.kallio@gmail.com (A.J.I.K.); hans-ole.orka@nmbu.no (H.O.Ø.); erik.naesset@nmbu.no (E.N.); terje.gobakken@nmbu.no (T.G.)

* Correspondence: michele.dalponte@fmach.it; Tel.: +39-0461-615596

Abstract: Wood decay caused by pathogenic fungi in Norway spruce forests causes severe economic losses in the forestry sector, and currently no efficient methods exist to detect infected trees. The detection of wood decay could potentially lead to improvements in forest management and could help in reducing economic losses. In this study, airborne hyperspectral data were used to detect the presence of wood decay in the trees in two forest areas located in Etnedal (dataset I) and Gran (dataset II) municipalities, in southern Norway. The hyperspectral data used consisted of images acquired by two sensors operating in the VNIR and SWIR parts of the spectrum. Corresponding ground reference data were collected in Etnedal using a cut-to-length harvester while in Gran, field measurements were collected manually. Airborne laser scanning (ALS) data were used to detect the individual tree crowns (ITCs) in both sites. Different approaches to deal with pixels inside each ITC were considered: in particular, pixels were either aggregated to a unique value per ITC (i.e., mean, weighted mean, median, centermost pixel) or analyzed in an unaggregated way. Multiple classification methods were explored to predict rot presence: logistic regression, feed forward neural networks, and convolutional neural networks. The results showed that wood decay could be detected, even if with accuracy varying among the two datasets. The best results on the Etnedal dataset were obtained using a convolution neural network with the first five components of a principal component analysis as input (OA = 65.5%), while on the Gran dataset, the best result was obtained using LASSO with logistic regression and data aggregated using the weighted mean (OA = 61.4%). In general, the differences among aggregated and unaggregated data were small.

Keywords: hyperspectral data; wood decay; forestry; classification; convolutional neural networks; forest health



Citation: Dalponte, M.; Kallio, A.J.I.; Ørka, H.O.; Næsset, E.; Gobakken, T. Wood Decay Detection in Norway Spruce Forests Based on Airborne Hyperspectral and ALS Data. *Remote Sens.* **2022**, *14*, 1892. <https://doi.org/10.3390/rs14081892>

Academic Editor: Eben Broadbent

Received: 11 March 2022

Accepted: 13 April 2022

Published: 14 April 2022

Publisher's Note: MDPI stays neutral with regard to jurisdictional claims in published maps and institutional affiliations.



Copyright: © 2022 by the authors. Licensee MDPI, Basel, Switzerland. This article is an open access article distributed under the terms and conditions of the Creative Commons Attribution (CC BY) license (<https://creativecommons.org/licenses/by/4.0/>).

1. Introduction

Forests are affected by many different pathogens. Fungal decay is a forest pathogen that is widely spread in Europe, causing the decomposition of organic material in living trees. Depending on the fungus present, different organic materials are affected [1]. It can be present in the roots, butt, or stem of the tree. In Norway, wood decay is widely spread and *Heterobasidion* spp., and *Armillaria* spp. are the fungi that cause around 80% of the wood decay damage [1]. A tree attacked by these fungi experiences a decay in the heartwood that becomes rot. The wood taken from the attacked trees has reduced value as it can only be used as pulpwood or as an energy source. Furthermore, infection caused by such fungi could also reduce the tree growth rate, leading to reduced carbon sequestration and less wood production [2].

Information regarding wood decay occurrence is essential for forest management and for reducing economic losses. A big challenge for early detection is that there are almost no external visual signs of wood decay [3], and thus, detection of the infection usually requires costly procedures like coring trees in the field. Moreover, such a manual procedure

cannot be extended over large areas. Remote sensing has been proposed as an approach to map extensive areas. There is substantial existing literature on the use of remote sensing to detect other diseases, pathogens, and stresses, like bark beetle infestations [4], nutrient levels reduction [5], and water stress [6]. As the wood decay usually does not affect the living ties of the trees, but only its core, it is more complex to detect as the tree could be under only limited stress. Nevertheless, some studies have shown that there is a difference in the crown density and structure between healthy trees and trees affected by wood decay [7,8], although this change is extremely difficult to note by visual inspection. Despite this, few studies have been carried out using remotely sensed data acquired from aerial or satellite platforms to detect wood decay [9–12]. Kankaanhuhta et al. [9] obtained a detection rate of healthy trees between 72% and 90%, and of infected trees between 94% and 96% when using bi-temporal hyperspectral images with 1.6 m spatial resolution and with 30 spectral channels in a forest area in Finland. Rätty et al. [11] predicted the volume of trees affected by wood decay in a spruce forest in Norway using harvester, remotely sensed, and environmental data. They found that remotely sensed predictor variables obtained from airborne laser scanning data and Sentinel-2 imagery were more important than the environmental variables in predicting wood decay volume. Allen et al. [12] explored the use of airborne hyperspectral data to predict wood decay presence in trees in Norway. Their experiments showed that it is possible to predict wood decay presence at tree level with a certain level of accuracy, leaving a margin for improvement.

As wood decay is a phenomenon that appears in individual trees, the most obvious way to map it would be to work at individual tree crown (ITC) level. When dealing with ITC-level analyses, features from remote sensing data are usually extracted for each ITC. The most common and effective data source used in the literature to delineate ITCs is airborne laser scanning (ALS) data, because such data enable large detection accuracies of individual trees and accurate delineation of the tree crowns compared to other remotely sensed data [13,14]. Moreover, with ITCs detected with ALS data, it is possible to help the field work of the harvester by optimizing the mapping of the skit trail network [15]. On the other hand, ALS data are not so effective in describing the physiological characteristics of trees or their health status, which are better captured by spectral data, in particular, hyperspectral data [16–19]. Hyperspectral data have been used in the literature to map tree diseases and insect outbreaks [17,18]. To combine the ITCs derived from ALS data with the spectral information of the hyperspectral imagery, the pixels of the images are usually aggregated inside each crown with different techniques [20]. This is done because the most frequently used classification methods, such as random forest or support vector machines, deal with each observation independently without accounting for the surrounding context. Such individual observations could be either an individual pixel or an aggregated group of pixels. The aggregation of the pixels inside the ITCs could be carried out in multiple ways, but scientific evidence in existing literature is sparse and mainly related to tree species classification [20]. Furthermore, the aggregation could lead to a loss of information, and thus it would be interesting to explore classification methods that deal with all the pixels inside an ITC and not with an aggregation of them. In recent years, much attention has been devoted to the use of deep learning methods [21–26] and, in particular, convolutional neural networks (CNN) [24,27–29]. These types of classification networks allow the exploitation of both the spectral and spatial information, which may improve the classification results substantially [27]. Indeed, these classifiers do not only utilize the individual pixel information but also the information inherent in surrounding pixels. Thus, they could be a means of exploiting the spectral information inside each individual ITC in a novel way.

The current study had two main objectives: (i) to analyze if hyperspectral data could be used to predict wood decay occurrence in Norway spruce trees; and (ii) to explore the best way to deal with the hyperspectral information inside each individual ITC in the context of wood decay occurrence prediction.

2. Data Sets Description

The study was conducted on two study sites located in southeastern Norway characterized by different altitudes, species compositions, and wood decay occurrence rate.

2.1. Dataset I: Etnedal

The study area is in the municipality of Etnedal, covering 470 ha, at an elevation between 300 and 700 m above sea level (Figure 1). The forest cover is dominated by Norway spruce (*Picea abies* (L.) Karst.), with presence of Scots pine (*Pinus sylvestris* L.) and birch (*Betula* spp. L.).

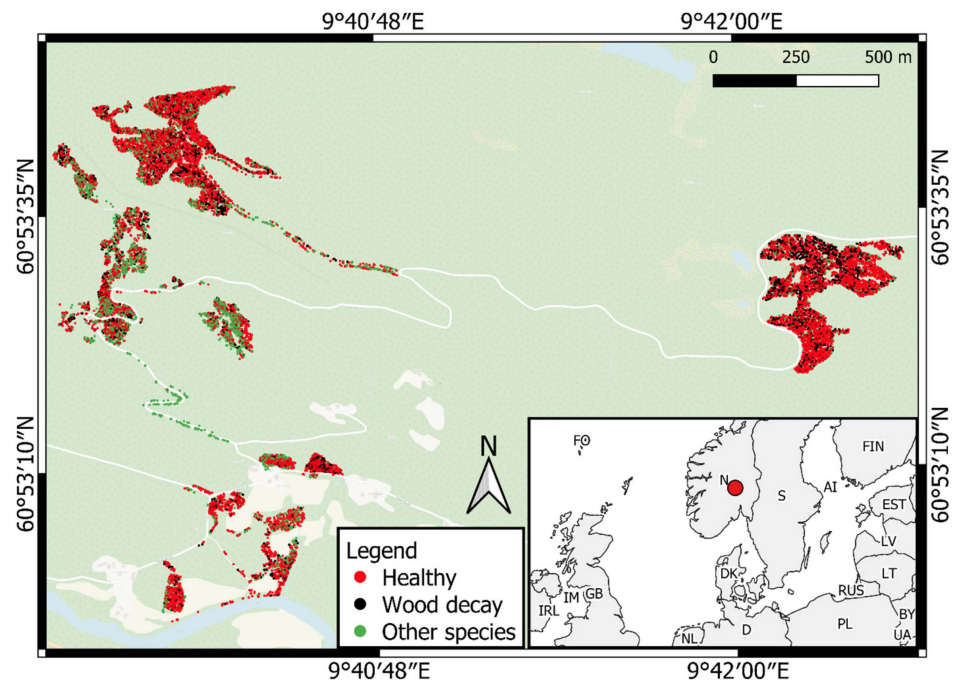


Figure 1. Dataset I: Location of the individual field trees (dots in the large map), and location of the study area (red dot in the inset).

Hyperspectral data were collected on the 3 August 2019 using the VNIR-1800 and SWIR-384 airborne HySpex sensors operating in the VNIR (400–990 nm) and SWIR (960–2520 nm) spectral ranges, respectively. The spatial resolution of the VNIR data was 0.3 m and for the SWIR, 0.7 m. The number of acquired bands was 186 for the VNIR sensor and 288 for the SWIR. Multiple strips were collected in order to cover the entire area. ALS data were collected during the same flight with a point density of 17.6 pts/m² using the Leica ALS70-HP system.

Field data were acquired during the harvesting using a cut-to-length harvester equipped with accurate positioning systems [30]. The mean positioning error at the single-tree level is expected to be smaller than 1 m. The ground reference data (Figure 1) contain 16,210 trees among which the majority were Norway spruce (13,488 trees), followed by Scots pine (1832 trees), and broadleaves species (890 trees). Among the Norway spruce trees, 3015 (22%) suffer from wood decay. The wood decay registrations were done during harvesting by the harvester operator classifying the trees. In greater detail, for each harvested tree, the operator registered if the trunk at the stump level was affected by wood decay. Single tree information, such as the diameters along the stem, were registered automatically by the harvester. The stump diameter of the trees ranged from a minimum of 6.0 cm to a maximum of 75.6 cm, with an average of 26.3 cm.

2.2. Dataset II: Gran

The study area is located in the municipality of Gran, and it covers an area of about 10,000 ha (Figure 2). The elevation is in the range of 200–500 m above sea level. The forest cover is dominated by Norway spruce, 20% by Scots pine and 5% by deciduous species.

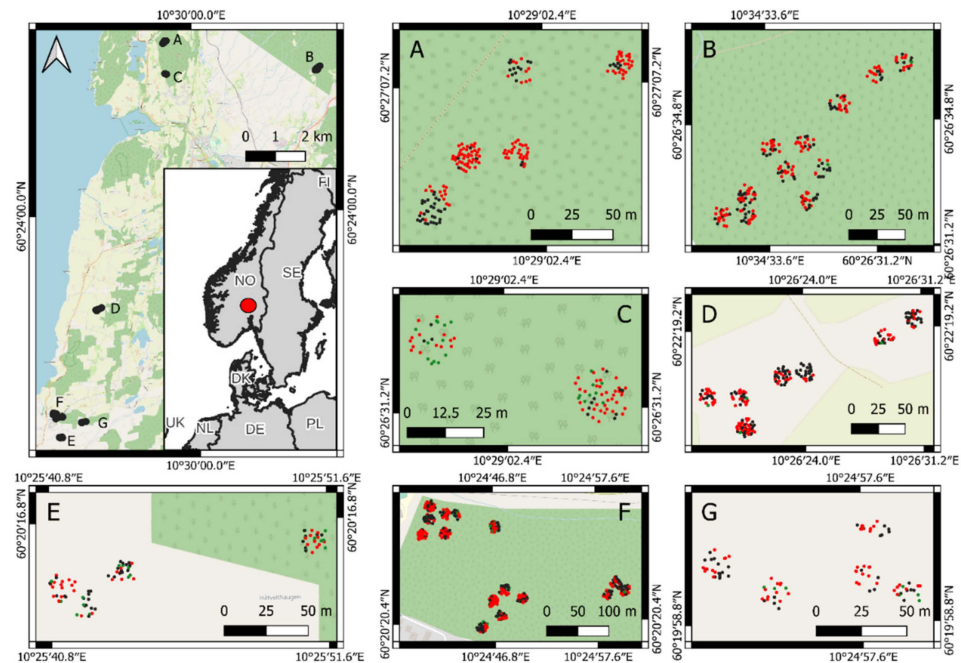


Figure 2. Dataset II: In the top left image: location of the field plots (black dots), and location of the study area in Norway (red dot). In the other images: location of the trees within the plots (red = healthy Norway spruce trees, black = wood decay-infected Norway spruce trees, green = other species) for the different locations (A–G).

Hyperspectral data were collected on the 11 August 2016 using the same sensors used in Dataset I. In this dataset, the spatial resolution of the VNIR data was 0.4 m and 1.0 m for SWIR. Multiple strips were collected in order to cover the entire area. The ALS data were acquired during summer 2015, with a point density of 5 pts/m².

The ground reference data (Figure 2) were collected in summer 2018 by manual field work: 49 circular sample plots of 250 m² in size were distributed in seven stands where clear-cuts were carried out after the remote sensing acquisition. In each plot, all stumps were registered, a fresh cut was made by chain saw, and the diameter of the stump and of the wood decay were calipered. For each stump, the position was registered with a TOPCON HiPer SR [31]. Each registration was done in a fixed position at the center of the stump. The horizontal root mean square error of the georeferencing ranged between 0.4 and 1.9 cm. All stumps were photographed with an Olympus TG-5 camera. The number of surveyed stumps was 1297, among which 1212 were Norway spruce trees, 73 deciduous species, and 12 Scots pine trees. Among the Norway spruce stumps, 497 (41%) were affected by wood decay. The stump diameters ranged from a minimum of 5.5 cm to a maximum of 60.4 cm, with an average value of 28.2 cm.

3. Methods

Figure 3 displays an overview of the methods used in this study. In the following paragraphs, each step is detailed.

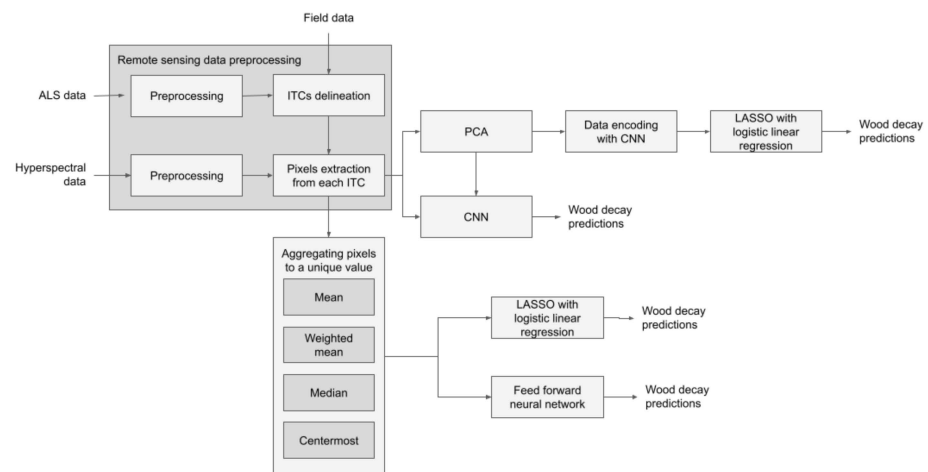


Figure 3. Overview of the methods adopted.

3.1. Remote Sensing Data Preprocessing

Hyperspectral images were mosaicked and radiometrically normalized in order to reduce the possible radiance differences among the strips. The normalization method proposed in [32] was used: each pixel was divided by its mean spectral value over all the bands. All the VNIR bands were considered, while in the SWIR images, some bands had a large number of missing values, and they were therefore discarded from the analysis. The final number of bands was 329 for Dataset I and 321 for Dataset II.

The ALS point cloud was normalized to create a canopy height model (CHM) using a DTM generated by the triangulated irregular network algorithm in the *normalize_height* function of the R package *lidR* [33]. The normalized ALS point cloud was used to detect the ITCs using the algorithm of Dalponte and Coomes [34] implemented in the function *itcLiDAR* of the R library *itcSegment* [35]. This algorithm is based on an adaptive local maxima filter and a region growing method, and it has been successfully used in many previous studies [34,36–39]. The delineated ITCs were linked to the field-measured trees by gradually searching the nearest pairs of tree crowns and ground reference data points until all pairs had been found [40]. However, if the distances were greater than 2 m, the pairs were excluded from the final dataset. For each ITC paired with a field data observation, the corresponding pixels in the hyperspectral images were extracted.

3.2. Pixels Aggregations

As each ITC varies in its size, a different number of hyperspectral pixels is available for each ITC. Thus, two different strategies were adopted to aggregate the information carried by these pixels. The first approach followed a standard method as all the pixels inside an ITC were reduced to a unique “representative” value for each band, while the second approach considered the pixels inside each ITC as a data cube. Both approaches are explained in the following subsections.

3.2.1. Aggregating the Pixels Inside Each ITC to a Representative Value

Traditional classification methods, such as support vector machines or random forest, require that the data points related to observations have the same dimension, which is not the case here since the number of pixels representing individual ITCs varies. To aggregate the values of the pixels related to each tree to one “representative” pixel per ITC, four aggregation strategies were tried and compared: (i) taking the mean over the pixels, (ii) taking the median over the pixels, (iii) using only the centermost pixels, and (iv) using a weighted mean where the pixels near to the center of the approximated tree crown have larger weights.

3.2.2. Representing the Data by Cubes

Aggregating the pixels corresponding to an ITC to a unique pixel may lead to information loss since the differences between the pixels may carry useful information. As an alternative approach, the pixels inside each ITC were represented as cubes. For each ITC, a matrix of 11×11 pixels centered on it was considered, and thus a cube of $11 \times 11 \times Nb$ values (i.e., Nb is the total number of available hyperspectral bands in each dataset considered) was obtained. In addition, an 11×11 layer that contained binary values indicating whether the pixel is inside or outside the ITC was added. The cubes therefore contained $11 \times 11 \times (Nb + 1)$ values. In the spatial dimension, an 11×11 layer was considered large enough so that the ITC should fit to the data cubes.

3.3. Prediction on Aggregated Data

3.3.1. LASSO with Logistic Linear Regression

The aggregated data were used to construct a logistic regression model. Logistic regression is a statistical modeling technique that in its basic form uses a logistic function to model a binary dependent variable. A binary logistic model has a dependent variable with two possible values, such as pass/fail which is represented by an indicator variable, where the two values are labeled “0” and “1”. In the logistic model, the log-odds (the logarithm of the odds) for the value labeled “1” is a linear combination of one or more independent variables (“predictors”); the independent variables can each be a binary variable (two classes, coded by an indicator variable) or a continuous variable (any real value). Let us assume that the outcome (predicted variable) and predictors are denoted by Y and X , respectively, and the two classes of interest are denoted by $+$ and $-$, respectively. The conditional probability is modelled that the outcome Y is $+$, given that the input variables (predictors) are X . The conditional probability is denoted by $p(Y = + | X)$, which will be abbreviated as $p(X)$ since we know that we are referring to the positive outcome $Y = +$. As the probability of class membership is sought, we must ensure that the hypothesis function always lies between 0 and 1. The function assumed in logistic regression is:

$$p(X) = \frac{\exp^{\beta_0 + \beta_1 X}}{1 + \exp^{\beta_0 + \beta_1 X}} \quad (1)$$

where β_0 and β_1 are vectors with as many components as there are predictors. The problem is to find the values of β_0 and β_1 that results in a $p(X)$ that most accurately classifies all the observed data points—that is, those that belong to the positive class have a probability as close as possible to 1 and those that belong to the negative class have a probability as close as possible to 0. One way to frame this problem is to say that we wish to maximize the product of these probabilities, often referred to as the log likelihood:

$$L = \log \left(\prod_{i:Y_i=+} p(x_i) \prod_{j:Y_j=-} (1 - p(x_j)) \right) \quad (2)$$

where \prod represents the products over i and j , which run over the positive and negative classed points, respectively.

The values of the logistic regression coefficients β_0 and β_1 are found by minimising the negative log likelihood described in Equation (2). LASSO regularization works by adding a penalty term $|\beta_1|$ to the log likelihood function L . The quantity to be minimized is thus:

$$L + \lambda \sum |\beta_1| \quad (3)$$

where λ is a free parameter, which is usually selected in such a way that the resulting model minimizes the sample error. Typically, the optimal value of λ is found using grid search with cross-validation. The effect of the penalty term is to set these coefficients exactly

to zero, and thus LASSO regression works like a feature selector that selects the most important coefficients, i.e., those that are most predictive (and have the smallest p-values).

All the data processing was done using the R language [41] and the regression models were fit using the *glmnet* package [42]. The models were constructed for all the four aggregation methods.

3.3.2. Feed forward Neural Networks

A feedforward neural network is an artificial neural network wherein connections between the nodes do not form a cycle, but the information moves in only one direction, i.e., forward, from the input nodes, through the hidden nodes (if any), and to the output nodes. In this study, a multilayer perceptron (MLP) network was considered. An MLP consists of at least three layers of nodes: an input layer, a hidden layer, and an output layer. Since MLPs are fully connected, each node in one layer connects with a certain weight to every node in the following layer. Except for the input nodes, each node is a neuron that uses a nonlinear activation function. The basic element of an MLP is a perceptron, which is a linear classifier that classifies input by separating two categories with a straight line. Input is typically a feature vector x multiplied by weights w and added to an intercept b : $y = w \times x + b$. A perceptron produces a single output based on several real-valued inputs by forming a linear combination using its input weights and passing the output through a nonlinear activation function:

$$y = \varphi(w^T \times x + b) \quad (4)$$

where w denotes the vector of weights, x is the vector of inputs, b is the intercept, and φ is the non-linear activation function. In this study, the rectified linear unit (ReLU) function was used as an activation function:

$$f(x) = \max(0, x) \quad (5)$$

Learning occurs in the perceptron by changing connection weights after each piece of data is processed, based on the amount of error in the output compared to the expected result. MLP utilizes a supervised learning technique called backpropagation for training.

In this study, values of 32, 16, 8, and 1 as output dimensions of the hidden layers were explored. The final output was mapped to the interval $[0, 1]$ using a sigmoid function. The model was trained using an Adam optimizer with 40 epochs, a learning rate of 0.001, and a batch size of 15. The loss function is the negative log likelihood of Equation (2). The models were implemented using *PyTorch* [21]. The models were constructed for all four aggregation methods.

3.4. Prediction on Unaggregated Data

3.4.1. Convolutional Neural Networks

A CNN is a deep learning algorithm that can use images or data cubes as an input source, and which assigns importance (learnable weights and biases) to various aspects/objects in the image and is capable of differentiating aspects/objects from the other. A CNN consists of an input layer, hidden layers, and an output layer. In any feed-forward neural network, middle layers are called hidden because their inputs and outputs are masked by the activation function and final convolution. In a CNN, the hidden layers include layers that perform convolutions. Typically, this includes a layer that performs a dot product of the convolution kernel with the layer's input matrix. This product is usually the Frobenius inner product, and its activation function is commonly ReLU. As the convolution kernel slides along the input matrix for the layer, the convolution operation generates a feature map, which in turn contributes to the input of the next layer. This is followed by other layers such as pooling layers, fully connected layers, and normalization layers.

CNNs are known to perform well in some applications, especially when spatial patterns are present, including applications in vegetation remote sensing [27]. In our case, data consist of hyperspectral images of trees, in which pixels have spatial relationships,

and the bands have a natural frequency-based order. A CNN starts by extracting features from groups of nearby pixels and bands and thus it exploits the spatial relationships of the data. In addition, the same filters are used over all groups of pixels to extract features, which reduces the complexity of the model as less filters need to be learned. For a more detailed description of CNNs and their uses, we refer to [27].

In order to make the CNN models less sensitive to the orientation of the data, multiples of 90-degree rotations and mirroring of the data were done, and the predictions were calculated as means of these individual predictions. As input to the CNN classifier, both the original bands and the first five principal components of a PCA of the hyperspectral images were tested. The models were implemented using PyTorch [21].

3.4.2. Data Encoding with CNN and LASSO with Logistic Linear Regression

CNNs could also be used for dimensionality reduction. In particular, useful spatial aggregations can be learned instead of just aggregating the data using simple statistics, such as taking the mean or median of the band values over all pixels. The aggregation can be learned using autoencoders with convolutional layers. The idea is that an encoder and a decoder are trained at the same time so that the decoder can reconstruct the unaggregated data from the aggregated data as well as possible. The encoder is thus a CNN, but rather than outputting predictions, it converts the high dimensional input data cubes into low dimensional vectors. In the best case, this method could learn to represent the key characteristics of ITCs and at the same time remove noise from the data. The aggregation is done using only the ITCs and the hyperspectral data without using the ground reference data on the wood decay presence.

Before training the model, the number of bands was reduced to five dimensions by applying PCA to all the available hyperspectral bands. This was done specially to make it easier to calculate the reconstruction loss as otherwise certain frequency areas containing a lot of highly correlated bands could gain too much importance. While we now had fewer values for each pixel, our attempt still preserved the heterogeneity among pixels.

After PCA, the input for the encoders consisted of grids of 11×11 pixels with five bands as well as an additional 11×11 binary layer which was used to reflect whether the pixels in the grid were truly part of the detected ITCs. Using encoders, these $6 \times 11 \times 11$ -dimensional data points were transformed into low dimensional vectors. The experimented output dimensions were 5, 10, 15, 20, 25 and 30, and for each dimension, an own encoder was trained.

To obtain predictions, the aggregations were used as an input for a LASSO with logistic linear regression. To choose which of the experimented aggregation dimensions works the best, a cross validation was used to simultaneously select the best dimension and the lasso regularization parameter. These were then used to obtain predictions for the separate test data.

As the orientation of a tree in the hyperspectral images should not affect the prediction outcome, the predictions were averaged over 90-degree rotations and mirroring of the original image data to gain more robust results. Again, PyTorch was used to implement all these models.

3.5. Evaluation of the Performance of the Models

A 10-fold cross validation was used to evaluate the performances of the models. The data were split into ten folds which were spatially disjointed. Concerning Dataset I, a grid of $100 \text{ m} \times 100 \text{ m}$ was generated, for which each square was assigned to a fold. The grid was overlaid over the ITCs, and all the ITCs with their center inside a square were assigned to a fold. Regarding Dataset II, all the trees inside a plot were assigned to the same fold. In this way, the spatial correlation among trees for different folds was reduced. The same splitting was used in every experiment to ensure comparable results.

The accuracies were evaluated through the overall accuracy (OA), the kappa coefficient (KA), the producer's (PA), and user's (UA) accuracies, the mean class accuracy (MCA), and

the F1-score. The MCA is the average of the PAs. The F1-score was computed considering the wood decay class as the positive class. To calculate these statistics, it is necessary to turn the wood decay occurrence probabilities into labels, and for doing so a decision threshold was used. A decision threshold set for each model based on experience from initial calculations was used.

4. Results

4.1. Dataset I

The results of the analysis for Dataset I are shown in Tables 1–4. Looking at the results with the aggregated data, it can be noted that choice of method used to aggregate the pixels inside the ITCs has a very small effect on the results as the differences are very small. In terms of prediction method, the logistic linear regression with LASSO optimization provided the best results considering the overall metrics (F1-score, OA, KA, and MCA).

For the unaggregated data (Tables 3 and 4), the results using the CNN were slightly better compared to the aggregated data (Tables 1 and 2). The best results for Dataset I were obtained considering the CNN with the first five PCA components. The use of the data encoding yielded the least favorable results.

Table 1. Overall summary of the model performances with pixel aggregations for Dataset I.

Prediction Method	Aggregation	F1-Score	OA (%)	KA	MCA (%)	PAs (%)		UAs (%)	
						Healthy	Wood Decay	Healthy	Wood Decay
LASSO with logistic linear regression	Mean	0.398	63.5	0.159	59.9	66.4	53.3	82.9	31.8
	Weighted mean	0.397	63.7	0.158	59.8	66.8	52.8	82.9	31.8
	Median	0.396	63.7	0.141	59.7	67.0	52.5	82.8	31.8
	Centermost pixel	0.385	62.7	0.160	58.8	65.9	51.6	82.3	30.7
Feedforward neural network	Mean	0.382	61.9	0.133	58.3	64.9	51.8	82.1	30.2
	Weighted mean	0.377	60.9	0.123	57.8	63.5	52.1	81.9	29.5
	Median	0.382	60.3	0.125	58.1	62.1	54.1	82.2	29.5
	Centermost pixel	0.354	58.6	0.087	55.6	61.1	50.1	80.7	27.4

Table 2. Confusion matrices of the models with pixel aggregations for Dataset I. The cells with gray background are the main diagonal of the confusion matrices.

LASSO with Logistic Linear Regression								
	Mean		Weighted Mean		Median		Centermost Pixel	
	Healthy	Wood Decay	Healthy	Wood Decay	Healthy	Wood Decay	Healthy	Wood Decay
Healthy	3749	781	3904	819	3774	785	3714	799
Wood decay	1887	871	1732	833	1862	867	1922	853
Feedforward Neural Network								
	Mean		Weighted mean		Median		Centermost pixel	
	Healthy	Wood decay	Healthy	Wood decay	Healthy	Wood decay	Healthy	Wood decay
Healthy	3658	797	3580	791	3501	758	3445	825
Wood decay	1978	855	2056	861	2135	894	2191	827

Table 3. Overall summary of the model performances with un-aggregated pixels for Dataset I.

Prediction Method	Features Used	F1-Score	OA (%)	KA	MCA (%)	PAs (%)		UAs (%)	
						Healthy	Wood Decay	Healthy	Wood Decay
CNN	Hyperspectral bands	0.390	64.4	0.156	59.4	68.6	50.2	82.4	31.9
	PCA	0.416	65.5	0.189	61.5	68.9	54.1	83.7	33.8
Encoding with CNN + LASSO	PCA	0.392	58.4	0.127	58.6	58.2	59.0	82.9	29.3

Table 4. Confusion matrices of the models with un-aggregated pixels for Dataset I. The cells with gray background are the main diagonal of the confusion matrices.

	CNN				Encoding with CNN + LASSO with Logistic Linear Regression			
	Hyperspectral Bands		PCA		PCA			
	Healthy	Wood Decay	Healthy	Wood Decay	Healthy	Wood Decay	Healthy	Wood Decay
Healthy	3866	823	3884	759	3411	716		
Wood decay	1770	829	1752	893	2225	936		

4.2. Dataset II

The results obtained for Dataset II (Tables 5–8) follow similar trends as for Dataset I, although with a few differences. The main difference that can be noted in Table 5, is that the accuracies for this dataset were slightly greater compared to Dataset I. Regarding the aggregation technique, the centermost pixel showed to provide the less accurate results, while the mean and weighted mean produced the best results. In terms of the prediction method, the results were comparable between the two techniques considered. When assessing the results for the unaggregated data, it can be noted that the results were less favorable than both those obtained for the aggregated data as well as for Dataset I (Table 3).

Table 5. Overall summary of the model performances with pixel aggregations for Dataset II.

Prediction Method	Aggregation	F1-Score	OA (%)	KA	MCA (%)	PAs (%)		UAs (%)	
						Healthy	Wood Decay	Healthy	Wood Decay
LASSO with logistic linear regression	Mean	0.513	59.6	0.171	58.8	62.4	55.3	69.1	47.8
	Weighted mean	0.544	61.4	0.215	61.2	62.4	59.9	71.4	49.8
	Median	0.510	60.1	0.175	59.0	63.8	54.1	69.0	48.3
	Centermost pixel	0.506	62.0	0.198	59.9	69.2	50.6	69.2	50.6
Feedforward neural network	Mean	0.473	52.3	0.055	52.9	50.2	55.6	64.5	41.1
	Weighted mean	0.517	60.5	0.185	59.5	64.1	54.9	69.5	48.8
	Median	0.515	58.0	0.153	58.0	58.0	58.0	68.9	46.3
	Centermost pixel	0.542	57.0	0.161	58.8	51.0	66.5	70.9	45.8

Table 6. Confusion matrices of the models with pixel aggregations for Dataset II. The cells with gray background are the main diagonal of the confusion matrices.

LASSO with Logistic Linear Regression								
	Mean		Weighted Mean		Median		Centermost Pixel	
	Healthy	Wood Decay	Healthy	Wood Decay	Healthy	Wood Decay	Healthy	Wood Decay
Healthy	282	126	272	118	265	119	283	128
Wood decay	130	131	140	139	147	138	129	129
Feedforward Neural Network								
	Mean		Weighted mean		Median		Centermost pixel	
	Healthy	Wood decay	Healthy	Wood decay	Healthy	Wood decay	Healthy	Wood decay
Healthy	207	114	264	116	239	108	210	86
Wood decay	205	143	148	141	173	149	202	171

Table 7. Overall summary of the model performances with un-aggregated pixels for Dataset II.

Prediction Method	Features Used	F1-Score	OA (%)	KA	MCA (%)	PAs (%)		UAs (%)	
						Healthy	Wood Decay	Healthy	Wood Decay
CNN	Hyperspectral bands	0.544	57.7	0.171	59.2	52.7	65.8	71.1	46.4
	PCA	0.462	54.0	0.067	53.4	55.6	51.4	64.7	41.9
Encoding with CNN + LASSO with logistic linear regression	PCA	0.507	56.4	0.127	56.7	55.1	58.4	68.0	44.8

Table 8. Confusion matrices of the models with unaggregated pixels for Dataset II. The cells with gray background are the main diagonal of the confusion matrices.

	CNN				Encoding with CNN + LASSO with Logistic Linear Regression			
	Hyperspectral Bands		PCA		PCA			
	Healthy	Wood Decay	Healthy	Wood Decay	Healthy	Wood Decay	Healthy	Wood Decay
Healthy	217	88	242	133	227	107		
Wood decay	195	169	170	124	185	150		

5. Discussion

In this study, the possibility to predict the presence of wood decay in trees using hyperspectral data and different types of prediction techniques was explored. The results obtained showed that it is possible to detect wood decay with a certain level of accuracy and that there is a difference in the predictive performance among the strategies adopted in terms of preprocessing and modelling.

Regarding the difference between aggregated and unaggregated data, the results differ between the two datasets. For Dataset I, the best result was obtained when using unaggregated data (i.e., CNN + PCA), while for Dataset II, the aggregated data were showed to be more efficient. This difference could be related to the fact that the size of the training sample in Dataset II is much smaller compared to Dataset I. In any case, in general, aggregated data seem to provide slightly better results, and this is probably because the wood decay presence is not much related to the spatial distribution of the values of the pixels covering the crown but to the general level of the values of the pixels of the crown. Concerning the aggregation strategy, it seems that it has a small effect on the results: the weighted mean performed slightly better than the others. It is worth noting that while the mean and the median are probably less sensitive to misalignments among ALS and hyperspectral data, the weighted mean and the centermost pixel value could be more sensitive.

The two datasets differ in terms of number of field sample trees, the way the trees were selected, the amount of wood decay in the trees, and the characteristics of the respective areas. In Dataset II, for which the amount of wood decay presence was larger, and the field data were collected after the harvesting with manual field survey, and the results were slightly better. This is interesting as this dataset also covers a larger area compared to Dataset I, for which all the trees were confined in a smaller area and thus there could be higher spatial correlation among the spectral values of the trees. However, the georeferencing of the trees was more accurate for Dataset II compared to Dataset I. The two datasets were also slightly different in terms of tree sizes, as described above. Considering only the trees matched with an ITC (and thus analyzed in this study), Dataset II was characterized by taller ITCs with larger stump diameters compared to Dataset I. The average stump diameter was 30.9 cm and 31.2 cm in Datasets I and II, respectively. Corresponding average ITC heights were 18.7 m and 22.3 m.

The wood decay detection did not reach a very high level of accuracy. This could be due to the complexity of the problem. Indeed, there are no visual signs of wood decay on trees that could be noticed in the field by the human eye without coring the trees. Some slight differences are visible in the spectral signatures as shown in Figure 4. As it can be seen, there are some slight differences among healthy and wood decay trees in some bands, but these differences are not enough for a clear separation among the two classes. The results obtained by this study are in line with a similar work published for one of the two datasets analyzed here [12]. Additionally, there may be multiple sources of noise in the data. The wood decay has been assessed only in binary categories (i.e., presence, absence) and thus there could be differences in the spectral signatures between trees with very high presence of wood decay and trees with little presence. Moreover, the results could be influenced by the age of the trees (older trees are more subject to wood decay than young trees) and other stresses to which the trees were subject and that were not measured in the field. These problems need to be addressed in the future taking additional information in the field, and expanding the study to other areas, with larger datasets. In any case, it is worth noting that Dataset I is already quite large compared to the standard ITCs studies present in the literature.

Even if in the literature very few studies exist on the detection of Norway spruce trees affected by wood decay (i.e., [11,12]), some studies could be found that deal with similar problems on other tree species. In [43], WorldView-2 data and ALS data were used to classify defoliation levels in *Quercus ilex* L. affected by wood decay. The classification accuracy for the defoliation ranged between 85.1% and 86.7%, with a kappa accuracy of 0.48–0.73. This task is different than the direct detection of wood decay presence, as in this case the task was simplified by visual signs of the infection on the tree crowns. Similarly, several studies can be found in the context of precision agriculture, where satellite data such as Sentinel-2 or Landsat have been used to detect wood decay in cotton and avocado [5,44–46]. In [47], the presence of wood decay in oil palms was classified according to the severity of infection, and the authors obtained classification accuracies greater than 90%. In this case, the task was again simplified by the fact that the type of fungi considered could kill an oil palm tree quite quickly (within 6–12 months) and cause severe yellowing of the foliage which is observable by humans during field inspection. Similarly, in a Douglas fir forest of British Columbia, Canada, Leckie et al. [48] classified the severity of wood decay infection using a multispectral sensor. Their classification scheme included eight classes, and they achieved a classification accuracy of 62.5%. Like in the previously cited studies, in this case, the task was advantaged by the fact that infected trees showed an extensive needle yellowing and defoliation, and even tree death.

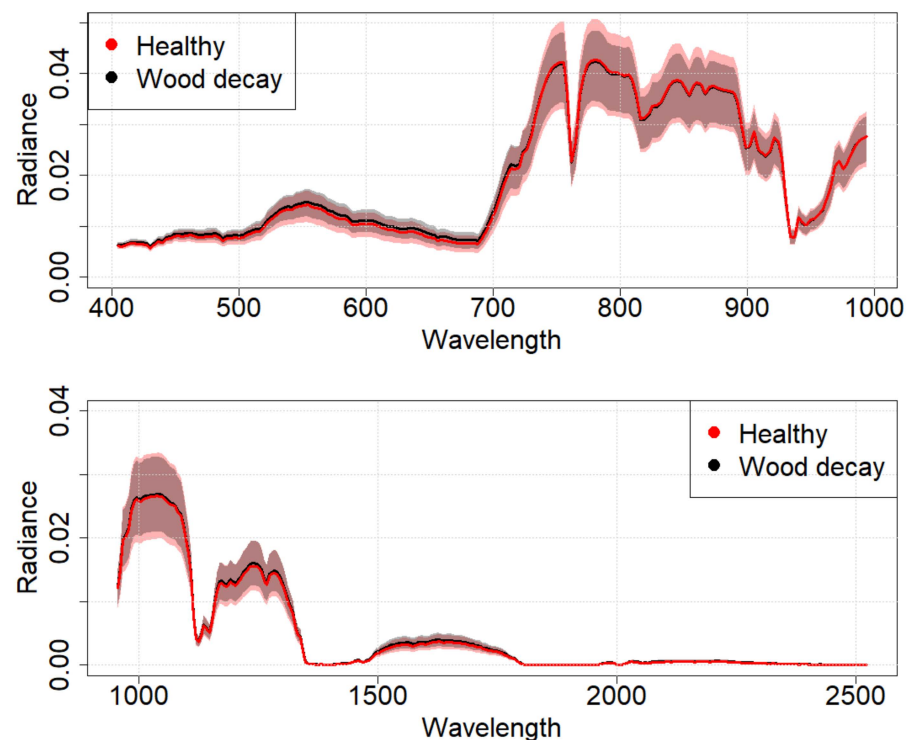


Figure 4. Spectral signatures of the healthy and wood decay ITCs in the Etnedal dataset using the mean pixel aggregations. The continuous line represents the median spectral signature while the box shows a range from the 25th to the 75th percentile.

6. Conclusions

The wood decay detection results are encouraging even if the detection errors are still quite high. The strategies adopted in terms of data aggregation and classification method used produced slightly different results: in a practical application, where the tradeoff between model simplicity and accuracy is important, it could be suggested to consider aggregated data using the weighted mean value of the pixels inside an ITC and the LASSO with logistic linear regression.

Author Contributions: Conceptualization, M.D., A.J.I.K., H.O.Ø., E.N. and T.G.; methodology, M.D. and A.J.I.K.; formal analysis, M.D. and A.J.I.K.; writing—original draft preparation, M.D. and A.J.I.K.; writing—review and editing, M.D., A.J.I.K., H.O.Ø., E.N. and T.G.; project administration, T.G.; funding acquisition, T.G. All authors have read and agreed to the published version of the manuscript.

Funding: This research was funded by the Research Council of Norway under the project PRECISION (NFR Project No. 281140).

Data Availability Statement: The data presented in this study may be available on request from the corresponding author.

Acknowledgments: We thank Øyvind Sørhuus for help in the field data collection. Furthermore, we would like to thank Terratec AS, Norway, for acquiring and processing the remotely sensed data, and Valdres Skog AS for permitting the use of their harvester data.

Conflicts of Interest: The authors declare no conflict of interest.

References

1. Solheim, H. Råtesopper—I Levende Trær. 2010. Available online: <http://hdl.handle.net/11250/2469366> (accessed on 12 April 2022).
2. Oliva, J.; Julio Camarero, J.; Stenlid, J. Understanding the Role of Sapwood Loss and Reaction Zone Formation on Radial Growth of Norway Spruce (*Picea Abies*) Trees Decayed by *Heterobasidion Annosum* s.l. *For. Ecol. Manag.* **2012**, *274*, 201–209. [CrossRef]
3. Vollbrecht, G.; Agestam, E. Identifying Butt Rotted Norway Spruce Trees from External Signs. *For. Landsc. Res.* **1995**, *1*, 241–254.

4. Meddens, A.J.H.; Hicke, J.A.; Vierling, L.A.; Hudak, A.T. Evaluating Methods to Detect Bark Beetle-Caused Tree Mortality Using Single-Date and Multi-Date Landsat Imagery. *Remote Sens. Environ.* **2013**, *132*, 49–58. [[CrossRef](#)]
5. Peng, Y.; Zhang, M.; Xu, Z.; Yang, T.; Su, Y.; Zhou, T.; Wang, H.; Wang, Y.; Lin, Y. Estimation of Leaf Nutrition Status in Degraded Vegetation Based on Field Survey and Hyperspectral Data. *Sci. Rep.* **2020**, *10*, 4361. [[CrossRef](#)] [[PubMed](#)]
6. Fensholt, R.; Huber, S.; Proud, S.R.; Mbow, C. Detecting Canopy Water Status Using Shortwave Infrared Reflectance Data From Polar Orbiting and Geostationary Platforms. *IEEE J. Sel. Top. Appl. Earth Obs. Remote Sens.* **2010**, *3*, 271–285. [[CrossRef](#)]
7. Pitkänen, T.P.; Piri, T.; Lehtonen, A.; Peltoniemi, M. Detecting Structural Changes Induced by Heterobasidion Root Rot on Scots Pines Using Terrestrial Laser Scanning. *For. Ecol. Manag.* **2021**, *492*, 119239. [[CrossRef](#)]
8. Žemaitis, P.; Žemaitė, I. Does Butt Rot Affect the Crown Condition of Norway Spruce Trees? *Trees* **2018**, *32*, 489–495. [[CrossRef](#)]
9. Kankaanhuhta, V.; Mäkisara, K.; Tomppo, E.; Piri, T.; Kaitera, J. Monitoring of Diseases Caused by Heterobasidion Annosum and Peridermium Pini in Norway Spruce and Scots Pine Stands by Airborne Imaging Spectrometry (AISA). In *Forest Condition Monitoring in Finland—National Report 1999*; Ukonmaanaho, L., Raitio, H., Eds.; Finnish Forest Research Institute: Parkano, Finland, 2000.
10. Ostovar, A.; Talbot, B.; Puliti, S.; Astrup, R.; Ringdahl, O. Detection and Classification of Root and Butt-Rot (RBR) in Stumps of Norway Spruce Using RGB Images and Machine Learning. *Sensors* **2019**, *19*, 1579. [[CrossRef](#)]
11. Rätty, J.; Breidenbach, J.; Hauglin, M.; Astrup, R. Prediction of Butt Rot Volume in Norway Spruce Forest Stands Using Harvester, Remotely Sensed and Environmental Data. *Int. J. Appl. Earth Obs. Geoinf.* **2021**, *105*, 102624. [[CrossRef](#)]
12. Allen, B.; Dalponte, M.; Hietala, A.M.; Ørka, H.O.; Næsset, E.; Gobakken, T. Detection of Root, Butt, and Stem Rot Presence in Norway Spruce with Hyperspectral Imagery. *Silva Fenn.* **2022**, *56*, 10606. [[CrossRef](#)]
13. Zhen, Z.; Quackenbush, L.; Zhang, L. Trends in Automatic Individual Tree Crown Detection and Delineation—Evolution of LiDAR Data. *Remote Sens.* **2016**, *8*, 333. [[CrossRef](#)]
14. Dalponte, M.; Reyes, F.; Kandare, K.; Gianelle, D. Delineation of Individual Tree Crowns from ALS and Hyperspectral Data: A Comparison among Four Methods. *Eur. J. Remote Sens.* **2015**, *48*, 365–382. [[CrossRef](#)]
15. Sterenczak, K.; Moskalik, T. Use of LIDAR-Based Digital Terrain Model and Single Tree Segmentation Data for Optimal Forest Skid Trail Network. *iForest* **2015**, *8*, 661–667. [[CrossRef](#)]
16. Doktor, D.; Lausch, A.; Spengler, D.; Thurner, M. Extraction of Plant Physiological Status from Hyperspectral Signatures Using Machine Learning Methods. *Remote Sens.* **2014**, *6*, 12247–12274. [[CrossRef](#)]
17. Liu, Y.; Zhan, Z.; Ren, L.; Ze, S.; Yu, L.; Jiang, Q.; Luo, Y. Hyperspectral Evidence of Early-Stage Pine Shoot Beetle Attack in Yunnan Pine. *For. Ecol. Manag.* **2021**, *497*, 119505. [[CrossRef](#)]
18. Xiong, D.; Huang, H.; Wang, Z.; Li, Z.; Tian, C. Assessment of Dwarf Mistletoe (*Arceuthobium Sichuanense*) Infection in Spruce Trees by Using Hyperspectral Data. *For. Path.* **2021**, *51*, e12669. [[CrossRef](#)]
19. Watt, M.S.; Leonardo, E.M.C.; Estarija, H.J.C.; Massam, P.; de Silva, D.; O’Neill, R.; Lane, D.; McDougal, R.; Buddenbaum, H.; Zarco-Tejada, P.J. Long-Term Effects of Water Stress on Hyperspectral Remote Sensing Indicators in Young Radiata Pine. *For. Ecol. Manag.* **2021**, *502*, 119707. [[CrossRef](#)]
20. Dalponte, M.; Ørka, H.O.; Ene, L.T.; Gobakken, T.; Næsset, E. Tree Crown Delineation and Tree Species Classification in Boreal Forests Using Hyperspectral and ALS Data. *Remote Sens. Environ.* **2014**, *140*, 306–317. [[CrossRef](#)]
21. Paszke, A.; Gross, S.; Massa, F.; Lerer, A.; Bradbury, J.; Chanan, G.; Killeen, T.; Lin, Z.; Gimelshein, N.; Antiga, L.; et al. PyTorch: An Imperative Style, High-Performance Deep Learning Library. *Adv. Neural Inf. Processing Syst.* **2019**, *32*, 1–12.
22. Hu, X.; Yuan, Y. Deep-Learning-Based Classification for DTM Extraction from ALS Point Cloud. *Remote Sens.* **2016**, *8*, 730. [[CrossRef](#)]
23. Mohan, A.; Singh, A.K.; Kumar, B.; Dwivedi, R. Review on Remote Sensing Methods for Landslide Detection Using Machine and Deep Learning. *Trans. Emerg. Telecommun. Technol.* **2021**, *32*, e3998. [[CrossRef](#)]
24. Maxwell, A.E.; Warner, T.A.; Guillén, L.A. Accuracy Assessment in Convolutional Neural Network-Based Deep Learning Remote Sensing Studies—Part 1: Literature Review. *Remote Sens.* **2021**, *13*, 2450. [[CrossRef](#)]
25. Osco, L.P.; Marcato Junior, J.; Marques Ramos, A.P.; de Castro Jorge, L.A.; Fatholahi, S.N.; de Andrade Silva, J.; Matsubara, E.T.; Pistori, H.; Gonçalves, W.N.; Li, J. A Review on Deep Learning in UAV Remote Sensing. *Int. J. Appl. Earth Obs. Geoinf.* **2021**, *102*, 102456. [[CrossRef](#)]
26. Yuan, X.; Shi, J.; Gu, L. A Review of Deep Learning Methods for Semantic Segmentation of Remote Sensing Imagery. *Expert Syst. Appl.* **2021**, *169*, 114417. [[CrossRef](#)]
27. Kattenborn, T.; Leitloff, J.; Schiefer, F.; Hinz, S. Review on Convolutional Neural Networks (CNN) in Vegetation Remote Sensing. *ISPRS J. Photogramm. Remote Sens.* **2021**, *173*, 24–49. [[CrossRef](#)]
28. Chen, L.; Li, S.; Bai, Q.; Yang, J.; Jiang, S.; Miao, Y. Review of Image Classification Algorithms Based on Convolutional Neural Networks. *Remote Sens.* **2021**, *13*, 4712. [[CrossRef](#)]
29. Sothe, C.; De Almeida, C.M.; Schimalski, M.B.; La Rosa, L.E.C.; Castro, J.D.B.; Feitosa, R.Q.; Dalponte, M.; Lima, C.L.; Liesenberg, V.; Miyoshi, G.T.; et al. Comparative Performance of Convolutional Neural Network, Weighted and Conventional Support Vector Machine and Random Forest for Classifying Tree Species Using Hyperspectral and Photogrammetric Data. *GIScience Remote Sens.* **2020**, *57*, 369–394. [[CrossRef](#)]

30. Noordermeer, L.; Sørngård, E.; Astrup, R.; Næsset, E.; Gobakken, T. Coupling a Differential Global Navigation Satellite System to a Cut-to-Length Harvester Operating System Enables Precise Positioning of Harvested Trees. *Int. J. For. Eng.* **2021**, *32*, 119–127. [[CrossRef](#)]
31. HiPer SR—Compact, Lightweight GNSS Receiver. Topcon Positioning Systems, Inc. Available online: <https://www.topconpositioning.com/gnss/integrated-gnss-receivers/hiper-sr> (accessed on 23 May 2021).
32. Yuan, D.; Elvidge, C.D. Comparison of Relative Radiometric Normalization Techniques. *ISPRS J. Photogramm. Remote Sens.* **1996**, *51*, 117–126. [[CrossRef](#)]
33. Roussel, J.-R.; Auty, D.; Coops, N.C.; Tompalski, P.; Goodbody, T.R.H.; Meador, A.S.; Bourdon, J.-F.; de Boissieu, F.; Achim, A. LidR: An R Package for Analysis of Airborne Laser Scanning (ALS) Data. *Remote Sens. Environ.* **2020**, *251*, 112061. [[CrossRef](#)]
34. Dalponte, M.; Coomes, D.A. Tree-Centric Mapping of Forest Carbon Density from Airborne Laser Scanning and Hyperspectral Data. *Methods Ecol. Evol.* **2016**, *7*, 1236–1245. [[CrossRef](#)] [[PubMed](#)]
35. Dalponte, M. ItcSegment: Individual Tree Crowns Segmentation. 2018. Available online: <https://cran.r-project.org/web/packages/itcSegment/index.html> (accessed on 12 April 2022).
36. Coomes, D.A.; Dalponte, M.; Jucker, T.; Asner, G.P.; Banin, L.F.; Burslem, D.F.R.P.; Lewis, S.L.; Nilus, R.; Phillips, O.L.; Phua, M.-H.; et al. Area-Based vs Tree-Centric Approaches to Mapping Forest Carbon in Southeast Asian Forests from Airborne Laser Scanning Data. *Remote Sens. Environ.* **2017**, *194*, 77–88. [[CrossRef](#)]
37. Coomes, D.A.; Šafka, D.; Shepherd, J.; Dalponte, M.; Holdaway, R. Airborne Laser Scanning of Natural Forests in New Zealand Reveals the Influences of Wind on Forest Carbon. *For. Ecosyst.* **2018**, *5*, 10. [[CrossRef](#)]
38. Dalponte, M.; Ene, L.T.; Marconcini, M.; Gobakken, T.; Næsset, E. Semi-Supervised SVM for Individual Tree Crown Species Classification. *ISPRS J. Photogramm. Remote Sens.* **2015**, *110*, 77–87. [[CrossRef](#)]
39. Versace, S.; Gianelle, D.; Frizzera, L.; Tognetti, R.; Garfi, V.; Dalponte, M. Prediction of Competition Indices in a Norway Spruce and Silver Fir-Dominated Forest Using Lidar Data. *Remote Sens.* **2019**, *11*, 2734. [[CrossRef](#)]
40. Zhao, K.; Suarez, J.C.; Garcia, M.; Hu, T.; Wang, C.; Londo, A. Utility of Multitemporal Lidar for Forest and Carbon Monitoring: Tree Growth, Biomass Dynamics, and Carbon Flux. *Remote Sens. Environ.* **2018**, *204*, 883–897. [[CrossRef](#)]
41. R: The R Project for Statistical Computing. Available online: <https://www.r-project.org/> (accessed on 26 April 2021).
42. Friedman, J.H.; Hastie, T.; Tibshirani, R. Regularization Paths for Generalized Linear Models via Coordinate Descent. *J. Stat. Softw.* **2010**, *33*, 1–22. [[CrossRef](#)]
43. Navarro-Cerrillo, R.M.; Varo-Martínez, M.Á.; Acosta, C.; Palacios Rodríguez, G.; Sánchez-Cuesta, R.; Ruiz Gómez, F.J. Integration of WorldView-2 and Airborne Laser Scanning Data to Classify Defoliation Levels in Quercus Ilex L. Dehesas Affected by Root Rot Mortality: Management Implications. *For. Ecol. Manag.* **2019**, *451*, 117564. [[CrossRef](#)]
44. Pérez-Bueno, M.L.; Pineda, M.; Vida, C.; Fernández-Ortuño, D.; Torés, J.A.; de Vicente, A.; Cazorla, F.M.; Barón, M. Detection of White Root Rot in Avocado Trees by Remote Sensing. *Plant Dis.* **2019**, *103*, 1119–1125. [[CrossRef](#)]
45. Song, X.; Yang, C.; Wu, M.; Zhao, C.; Yang, G.; Hoffmann, W.C.; Huang, W. Evaluation of Sentinel-2A Satellite Imagery for Mapping Cotton Root Rot. *Remote Sens.* **2017**, *9*, 906. [[CrossRef](#)]
46. Wu, M.; Yang, C.; Song, X.; Hoffmann, W.C.; Huang, W.; Niu, Z.; Wang, C.; Li, W.; Yu, B. Monitoring Cotton Root Rot by Synthetic Sentinel-2 NDVI Time Series Using Improved Spatial and Temporal Data Fusion. *Sci. Rep.* **2018**, *8*, 2016. [[CrossRef](#)] [[PubMed](#)]
47. Lelong, C.C.; Roger, J.-M.; Brégrand, S.; Dubertret, F.; Lanore, M.; Sitorus, N.; Raharjo, D.; Caliman, J.-P. Evaluation of Oil-Palm Fungal Disease Infestation with Canopy Hyperspectral Reflectance Data. *Sensors* **2010**, *10*, 734–747. [[CrossRef](#)] [[PubMed](#)]
48. Leckie, D.G.; Jay, C.; Gougeon, F.A.; Sturrock, R.N.; Paradine, D. Detection and Assessment of Trees with Phellinus Weirii (Laminated Root Rot) Using High Resolution Multi-Spectral Imagery. *Int. J. Remote Sens.* **2004**, *25*, 793–818. [[CrossRef](#)]